Journal of Magnetic Resonance **155,** 263–277 (2002)
doi:10.1006/jmre.2002.2505, available online at http://www.idealibrary.com on IDEAL®

Obtaining Molecular and Structural Information from ^{13}C–^{14}N Systems with ^{13}C FIREMAT Experiments

Mark Strohmeier, D. W. Alderman, and David M. Grant[1]

Department of Chemistry, University of Utah, 315 S. 1400 E., Salt Lake City, Utah 84112-0850

E-mail: grant@chemistry.utah.edu

Received September 19, 2001; revised December 26, 2001

The effect of dipolar coupling to ^{14}N on ^{13}C FIREMAT (*five* π *re*plicated *m*agic *a*ngle *t*urning) experiments is investigated. A method is developed for fitting the ^{13}C FIREMAT FID employing the full theory to extract the ^{13}C–^{14}N dipolar and ^{13}C chemical shift tensor information. The analysis requires prior knowledge of the electric field gradient (EFG) tensor at the ^{14}N nucleus. In order to validate the method the analysis is done for the amino acids α-glycine, γ-glycine, *l*-alanine, *l*-asparagine, and *l*-histidine on FIREMAT FIDs recorded at ^{13}C frequencies of 50 and 100 MHz. The dipolar and chemical shift data obtained with this analysis are in very good agreement with the previous single-crystal ^{13}C NMR results and neutron diffraction data on α-glycine, *l*-alanine, and *l*-asparagine. The values for γ-glycine and *l*-histidine obtained with this new method are reported for the first time. The uncertainties in the EFG tensor on the resultant ^{13}C chemical shift and dipolar tensor values are assessed.

Key Words: **^{14}N dipolar coupling; ^{14}N quadrupolar coupling; chemical shift principal values; FIREMAT; amino acids.**

INTRODUCTION

The principal values of the chemical shift tensor are known to be sensitive to the local electronic environment and contain detailed information on the local three-dimensional electron distribution (*1*) It has been shown that principal values allow insights into the molecular conformation and the chemical environment that are unavailable from the isotropic chemical shift (*2–5*). Combined experimental and *ab initio* studies on small model peptides and terpenes revealed that the shift tensor principal values may be used for a detailed structural analysis and that this combination is a powerful method which may be utilized when suitable crystals for X-ray analysis are not available (*6–10*). However, these methods require accurate experimental principal shift values determined by reliable experimental methods.

Recent solid-state magic angle turning (MAT) 2D isotropic/anisotropic (I/A) experiments such as the FIREMAT experiment permit the measurement of chemical shift tensor principal values in powdered samples of large molecules (*11, 12*). These experiments separate the slow spinning sideband patterns arising from dilute, spin-1/2 nuclei such as ^{13}C according to their isotropic shifts. Usually the isotropic dimension of the spectrum exhibits high resolution, permitting analysis of signals whose isotropic shifts differ by as little as 0.2 ppm. The FIREMAT experiment applied to natural abundance samples will measure ^{13}C chemical shift tensor principal values in molecules with dozens of carbons. Complications arise, however, in the compounds of interest that incorporate nitrogen atoms, such as amino acids, DNA/RNA bases, natural products, drugs, and dyes. The quadrupolar interaction of the abundant spin-1 ^{14}N nucleus introduces terms into the ^{13}C–^{14}N dipolar coupling that are incompletely averaged by magic angle spinning (MAS) (*13*). This residual dipolar coupling to ^{14}N produces the well-known broad 2 : 1 doublet structure in the ^{13}C MAS spectrum. Such lineshapes can be tolerated in high-speed MAS experiments used to determine isotropic shifts, particularly when high fields are employed to minimize the quadrupolar effects. But the situation is much more complicated for the FIREMAT and other 2D I/A experiments designed to measure the chemical shift tensor principal values. Although the effect of ^{13}C–^{14}N dipolar coupling on 1D slow spinning experiments has been discussed earlier, its effect on the FIREMAT experiment has not been examined (*14*). As will be shown below, the effect of dipolar coupling to a ^{14}N nucleus is quite pronounced in ^{13}C FIREMAT experiments; both the isotropic and the anisotropic dimensions of the 2D FID are impacted by the ^{13}C–^{14}N dipolar coupling and the lineshapes in the two dimensions are correlated. In some previous work the sideband manifold was described by a model in which the ^{13}C–^{14}N dipolar coupling was included, but the ^{14}N quadrupolar coupling was thought to have a negligible effect (*6, 9*). Elsewhere the dipolar coupling to ^{14}N was not considered (*10, 15–17*). Such neglect precludes the reliable determination of chemical shift tensor principal values for carbons bonded to nitrogen and the ^{14}N quadrupolar interaction and ^{13}C–^{14}N coupling are required to obtain accurate chemical shift tensor principal values from FIREMAT and related experiments.

[1] To whom correspondence should be addressed.

1090-7807/02 $35.00

Coupling to ^{14}N is not entirely a liability, however, as previous static and variable-angle spinning 1D experiments have demonstrated that orientation information on the ^{13}C chemical shift tensor may be obtained from such data (*18–20, 49*). But the previous 1D methods are restricted to relatively small molecules with a limited number of resonances, since any overlap of the patterns complicates, or biases, the analysis. A complete analysis of the effects of residual dipolar coupling in the FIREMAT experiment, in which signals from different carbons are separated from one another, can provide chemical shift tensor orientation information in large molecules.

In this paper the effect of coupling to ^{14}N on the ^{13}C FIREMAT experiment is investigated. A method based on a full simulation of the FIREMAT FID that includes the effect of the ^{14}N quadrupolar interaction and the ^{13}C–^{14}N dipolar coupling is developed here. Fitting the experimental FIREMAT FID with the simulated 2D FIDs extracts the ^{13}C chemical shift tensor principal values, the ^{13}C–^{14}N dipolar coupling constant, and in favorable circumstances, the orientation of the ^{13}C–^{14}N internuclear vector in the chemical shift tensor principal axis system. The ^{14}N quadrupolar interaction described by the electric field gradient (EFG) tensor and the ^{14}N quadrupole moment is undetermined by the fitting of the FIREMAT FID; the EFG must be found separately, either from experiment or from computation, and supplied to the simulations.

The new spectral analysis developed here is used to obtain the ^{13}C chemical shift tensor principal values, the dipolar coupling constants, and the orientation of the ^{13}C–^{14}N internuclear vectors in the chemical shift principal axis system in α-glycine, γ-glycine, *l*-alanine, *l*-asparagine, and *l*-histidine. The analysis is done in the time domain on complete ^{13}C FIREMAT FIDs recorded at 50 and 100 MHz. The values obtained are compared with those available from previous ^{13}C single-crystal studies in order to assess the accuracy of the new method. The influence of uncertainty in the assumed ^{14}N EFG tensor on the ^{13}C chemical shift tensor principal values and the dipolar coupling constant is explored.

THEORY

In the following section it is outlined how the FIREMAT FID may be described for a rotating powder. In the second section the necessary spin quantum mechanics to calculate the FIREMAT FID for the ^{13}C–^{14}N spin system is discussed. The isotropic phase encoding of ^{14}N dipolar-coupled lines by the 5π pulses of the FIREMAT experiment is complicated and the details are presented in the Appendix. In order to substantiate that the 5π pulse sequence of the FIREMAT experiment correctly encodes ^{14}N-coupled ^{13}C isotropic shifts in the evolution dimension, the P2DSS (*p*seudo 2D sideband suppression) (*21*) spectrum and the high-speed MAS spectrum of *l*-histidine are compared and both are found to yield the same phase encoding, as shown in Fig. 1.

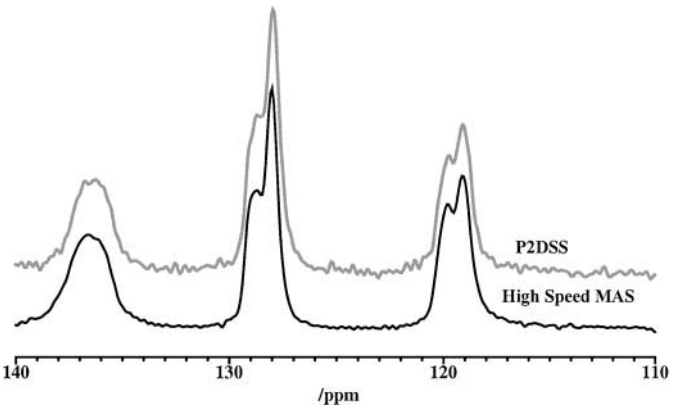

FIG. 1. Comparison of the *l*-histidine P2DSS ($\omega_r = 2\pi \cdot 500$ Hz) and high-speed CPMAS ($\omega_r = 2\pi \cdot 4000$ Hz) spectra in the aromatic isotropic shift region. Both spectra are taken at 4.7 T.

FIREMAT FID. The 1D spectrum of a single crystal rotating at the magic angle with angular frequency ω_r consists of sidebands of varying phase at frequencies $W_0 + k \cdot \omega_r$ with complex amplitudes a_k (*22*). The free induction decay (FID) of the complex magnetization of this rotating crystallite after a wide band $\pi/2$ pulse or cross polarization from protons may be expressed as

$$\rho_{1D}(\alpha, \beta, \gamma \mid t_2) = \sum_k a_k(\alpha, \beta, \gamma) \exp[-i(W_0(\alpha, \beta) + k \cdot \omega_r) \cdot t_2], \qquad [1]$$

where α, β, and γ are the three Euler angles rotating the laboratory frame into a frame fixed relative to the crystallite at $t = 0$. The rotation is depicted in Fig. 2, where the rotor axis **S** is defined to be the z axis of the laboratory frame; thus the magnetic field $\mathbf{B}_o$ is described by all three Euler angles and the magic angle. The complex sideband amplitudes are normalized by $\sum_k a_k(\alpha, \beta, \gamma) = 1$. The factor $W_0(\alpha, \beta)$ is the isotropic angular Larmor frequency around the γ circle. In the general case treated here $W_0(\alpha, \beta)$ is dependent on the rotor axis orientation

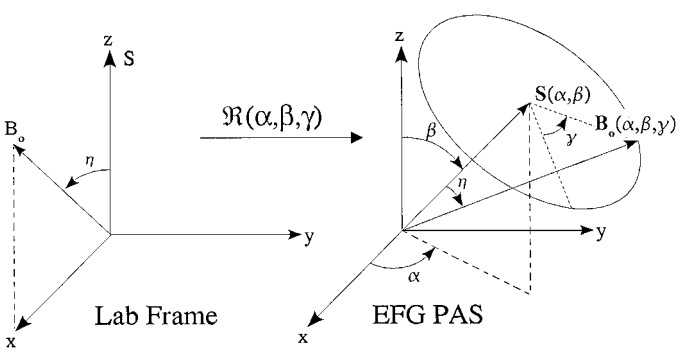

FIG. 2. Orientation of the spinner axis S and the Zeeman field B_o in the molecular EFG principal axis system.

α and β. Terms describing transverse relaxation will be added later since they are not necessary for the present discussion.

The 2D FID of a single crystallite in a complex phase-encoded FIREMAT experiment is written as

$$\rho_{2D}(\alpha, \beta, \gamma \mid t_1, t_2) = \exp[-i(W_0(\alpha, \beta)t_1] \cdot \rho_{1D}(\alpha, \beta, \gamma \mid t_2), \quad [2]$$

where $\exp[-iW_0(\alpha, \beta)t_1]$ represents the phase encoding of the isotropic frequency resulting from the t_1-dependent pulse sequence. The Appendix outlines how this phase encoding in the evolution dimension may be obtained with an experiment based on π pulses. Integrating Eq. [2] over the powder angles α, β, and γ gives the evolution of 2D FID $M_+(t_1, t_2)$ for a uniformly distributed powder

$$M_+(t_1, t_2) = \frac{M_o}{8\pi^2} \int_0^{2\pi} d\alpha \int_0^{\pi} \sin\beta \, d\beta \cdot \exp[-iW_0(\alpha, \beta)t_1] \cdot \int_0^{2\pi} d\gamma \rho_{1D}(\alpha, \beta, \gamma \mid t_2), \quad [3]$$

where M_o is the initial magnetization in the transverse plane. Substituting Eq. [1] into Eq. [3] and rearranging yield

$$M_+(t_1, t_2) = \frac{M_o}{4\pi} \int_0^{2\pi} d\alpha \int_0^{\pi} \sin\beta \, d\beta \cdot \exp[-iW_0(\alpha, \beta)t_1] \cdot \sum_k \exp[-i(W_0(\alpha, \beta) + k \cdot \omega_r)t_2] \cdot \frac{1}{2\pi} \int_0^{2\pi} d\gamma a_k(\alpha, \beta, \gamma). \quad [4]$$

The integral over γ of the complex sideband amplitudes $a_k(\alpha, \beta, \gamma)$ is positive and real (*14, 23*). Defining $A_k(\alpha, \beta)$ as the γ average of $a_k(\alpha, \beta, \gamma)$ and substituting yield

$$M_+(t_1, t_2) = \frac{M_o}{4\pi} \int_0^{2\pi} d\alpha \int_0^{\pi} \sin\beta \, d\beta \cdot \exp[-iW_0(\alpha, \beta)t_1] \cdot \sum_k A_k(\alpha, \beta) \cdot \exp[-i(W_0(\alpha, \beta) + k \cdot \omega_r)t_2]. \quad [5]$$

This 2D FID contains only integrals over the α and β powder angles and is used for the simulations. The sideband amplitudes $A_k(\alpha, \beta)$ may be calculated using the banded matrix approach, which requires the orientational dependent frequency function $\omega(\alpha, \beta, \gamma)$ expanded in a Fourier series around the γ angle (*14*):

$$\omega(\alpha, \beta, \gamma) = \sum_{m=-\infty}^{\infty} W_m(\alpha, \beta) \exp[i m\gamma]. \quad [6]$$

For purely second-rank interactions such as the chemical shift and the dipolar coupling between spin-1/2 nuclei all expansion coefficients W_m with $m > 2$ are zero. In addition, the average Larmor frequency over γ, $W_0(\alpha, \beta)$, is invariant under any rotation of α and β for second-rank interactions. However, for the dipolar coupling between a spin-1/2 and a quadrupolar nucleus higher order expansion coefficients $W_m(\alpha, \beta)$ with $m > 2$ can be nonzero and may have to be considered. Furthermore, the dipolar coupling between a spin-1/2 and a quadrupolar nucleus with spin ≥ 1 introduces higher rank quadrupolar terms into $W_0(\alpha, \beta)$ that depend on the powder angles α and β. This dependence is the source of the 2 : 1 doublets often observed in 1D high-speed MAS spectra of ^{13}C–^{14}N systems (*13*). Such inhomogeneous broadening in the isotropic dimension of the FIREMAT FID undermines the requirements of TIGER processing (*24*).

Spin quantum mechanics for the ^{13}C–^{14}N system. In order to obtain the frequency function $\omega(\alpha, \beta, \gamma)$ for a spin A in an AX spin system where nucleus A is spin-1/2 and nucleus X is spin ≥ 1, the Zeeman, quadrupole, chemical shift, and coupling interactions must be considered in the total Hamiltonian. This total Hamiltonian may be conveniently divided into the A zero-order Hamiltonian consisting of the A spin Zeeman (Z) term and the X spin zero-order Hamiltonian including both the Zeeman and quadrupolar (Q) terms. The perturbation Hamiltonian consists of the A spin chemical shift (CS), the dipolar (D), and scalar (J) coupling terms:

$$\hat{H}_{AX}^{total} = \underbrace{\hat{H}_A^Z}_{\hat{H}_A^0} + \underbrace{\hat{H}_X^Z + \hat{H}_X^Q}_{\hat{H}_X^0} + \underbrace{\hat{H}_A^{CS} + \hat{H}_{AX}^D + \hat{H}_{AX}^J}_{\hat{H}_{AX}^{pert}}. \quad [7]$$

Diagonalization of the zero-order Hamiltonians yields the zero-order wavefunctions, which are applied to the perturbing Hamiltonian yielding the first-order energy shift. The frequency function for the A spin transition is then obtained from the energy difference between states with the same X spin states.

The choice of reference system does not affect the result. Here the EFG principal axis system (PAS) is chosen as the crystallite-fixed reference axis system since simpler expressions are obtained. The coupling and chemical shift Hamiltonians are expressed in this system. The transformation strategy with the corresponding angles is shown in Fig. 3. In the following part the spin quantum mechanics in the EFG PAS, including explicit expressions for all Hamiltonians in SI energy units, is briefly described (*25, 26*).

The normalized $\mathbf{B}_o$ field direction defined by the Euler angles α, β, and γ may be expressed in the EFG PAS by the directional

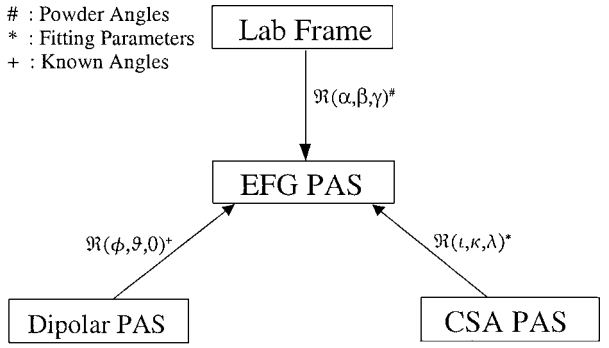

FIG. 3. Outline of the transformation strategy. All spin quantum mechanics are done in the EFG PAS.

cosines:

$$\begin{pmatrix} b_x \\ b_y \\ b_z \end{pmatrix} = \begin{pmatrix} \sqrt{\frac{2}{3}}\cos\alpha\cos\beta\cos\gamma + \sqrt{\frac{1}{3}}\cos\alpha\sin\beta - \sqrt{\frac{2}{3}}\sin\alpha\sin\gamma \\ \sqrt{\frac{2}{3}}\sin\alpha\cos\beta\cos\gamma + \sqrt{\frac{1}{3}}\sin\alpha\sin\beta + \sqrt{\frac{2}{3}}\cos\alpha\sin\gamma \\ -\sqrt{\frac{2}{3}}\sin\beta\cos\gamma + \sqrt{\frac{1}{3}}\cos\beta \end{pmatrix}. \quad [8]$$

The A and X Zeeman Hamiltonians in the EFG PAS are then given by

$$\hat{H}^{\mathrm{Z}}_{\mathrm{A}}(\alpha,\beta,\gamma) = -\hbar\gamma_{\mathrm{A}}B_{\mathrm{o}}(b_x b_y b_z)\begin{pmatrix} \hat{I}_x \\ \hat{I}_y \\ \hat{I}_z \end{pmatrix} \quad [9a]$$

$$\hat{H}^{\mathrm{Z}}_{\mathrm{X}}(\alpha,\beta,\gamma) = -\hbar\gamma_{\mathrm{X}}B_{\mathrm{o}}(b_x b_y b_z)\begin{pmatrix} \hat{S}_x \\ \hat{S}_y \\ \hat{S}_z \end{pmatrix}, \quad [9b]$$

where $\hat{I}$ and $\hat{S}$ are the A and X spin operators, respectively. The quadrupolar Hamiltonian in its PAS is

$$\hat{H}^{\mathrm{Q}}_{\mathrm{X}} = \frac{\chi\cdot h}{4S(2S-1)}\left[3\left(\hat{S}_z^2 - \hat{S}^2\right) + \frac{1}{2}\eta_{\mathrm{EFG}}(\hat{S}^+\hat{S}^+ - \hat{S}^-\hat{S}^-)\right], \quad [10]$$

where χ is the quadrupolar coupling constant and η_{EFG} is the asymmetry of the EFG tensor. They are defined by

$$\chi = e^2 Q q_{\mathrm{o}}/h \quad \text{with } eq_{\mathrm{o}} = V_{zz}, \quad \text{and } \eta_{\mathrm{EFG}} = \frac{V_{xx}-V_{yy}}{V_{zz}},$$

where the principal values of the EFG tensor are ordered with the convention $|V_{xx}| < |V_{yy}| < |V_{zz}|$. The chemical shift Hamiltonian for spin A is expressed by

$$\hat{H}^{\mathrm{CS}}_{\mathrm{Z}}(\alpha,\beta,\gamma) = -\hbar 10^{-6}\gamma_{\mathrm{A}}B_{\mathrm{ref}}\cdot(b_x b_y b_z)\Re(\iota,\kappa,\lambda) \times \begin{pmatrix} \delta_{11} & 0 & 0 \\ 0 & \delta_{22} & 0 \\ 0 & 0 & \delta_{33} \end{pmatrix}\Re(\iota,\kappa,\lambda)^{-1}\begin{pmatrix} \hat{I}_x \\ \hat{I}_y \\ \hat{I}_z \end{pmatrix}, \quad [11]$$

where $\Re(\iota,\kappa,\lambda)$ is the transformation matrix that rotates the shift tensor into the EFG PAS. The rotation is specified by three Euler angles ι, κ, λ. The convention $\delta_{11} > \delta_{22} > \delta_{33}$ is used for the principal shift values, and $\gamma_{\mathrm{A}}B_{\mathrm{ref}}$ is the reference frequency. The dipolar coupling Hamiltonian for an arbitrary internuclear vector specified by the polar angles θ and ϕ in the EFG PAS is given by

$$\begin{aligned}\hat{H}^{\mathrm{D}}_{\mathrm{AX}} = Dh\Bigg[&(1-3\cos^2\theta)\left(\hat{I}_z\hat{S}_z - \frac{1}{4}(\hat{I}^+\hat{S}^- + \hat{I}^-\hat{S}^+)\right) \\ &- \frac{3}{2}\sin\theta\cos\theta((\hat{I}^+\hat{S}_z + \hat{I}_z\hat{S}^+)e^{-i\phi} + (\hat{I}^-\hat{S}_z + \hat{I}_z\hat{S}^-)e^{i\phi}) \\ &- \frac{3}{4}\sin^2\theta(\hat{I}^+\hat{S}^+e^{-i2\phi} + \hat{I}^-\hat{S}^-e^{i2\phi})\Bigg], \end{aligned} \quad [12]$$

where D is the dipolar coupling constant defined by $Dh = (\gamma_{\mathrm{A}}\gamma_{\mathrm{X}}\hbar^2/r^3_{\mathrm{AX}})\cdot(\mu_{\mathrm{o}}/4\pi)$. The scalar coupling with coupling constant J is written as

$$\hat{H}^{\mathrm{J}}_{\mathrm{AX}} = hJ(\hat{I}_x\hat{I}_y\hat{I}_z)\begin{pmatrix} \hat{S}_x \\ \hat{S}_y \\ \hat{S}_z \end{pmatrix} \quad [13]$$

It should be noted at this point that the quadrupolar and coupling Hamiltonians are independent of the $\mathbf{B}_{\mathrm{o}}$ direction; the orientational dependence is introduced only by the Zeeman and shift terms. Although the above Hamiltonians are applicable to any X spin, what follows will be written for the X nucleus having spin-1.

The zero-order eigenstates of the A spin system are readily obtained from the zero-order Hamiltonian $\hat{H}^{\mathrm{o}}_{\mathrm{A}}(\alpha,\beta,\gamma)$ by 2×2 matrix diagonalization so that

$$\begin{aligned} E^{\mathrm{A}}_f &= \left\langle\phi^{\mathrm{A}}_f(\alpha,\beta,\gamma)\middle|\hat{H}^{\mathrm{o}}_{\mathrm{A}}(\alpha,\beta,\gamma)\middle|\phi^{\mathrm{A}}_f(\alpha,\beta,\gamma)\right\rangle, \\ f &= \{1,2\}, \quad \text{where } E_1 > E_2 \end{aligned} \quad [14]$$

and similarly the X eigenstates by 3×3 matrix diagonalization $\hat{H}^{\mathrm{o}}_{\mathrm{X}}(\alpha,\beta,\gamma)$, giving

$$\begin{aligned} E^{\mathrm{X}}_g(\alpha,\beta,\gamma) &= \left\langle\phi^{\mathrm{X}}_g(\alpha,\beta,\gamma)\middle|\hat{H}^{\mathrm{o}}_{\mathrm{X}}(\alpha,\beta,\gamma)\middle|\phi^{\mathrm{X}}_g(\alpha,\beta,\gamma)\right\rangle, \\ g &= \{1,2,3\}, \quad \text{where } E_1 > E_2 > E_3. \end{aligned} \quad [15]$$

These diagonalizations yield the exact A and X zero-order eigenfunctions as linear combinations of the spin basis functions in the EFG PAS:

$$\left|\phi_f^{\mathrm{A}}(\alpha,\beta,\gamma)\right\rangle = c_{+\frac{1}{2}f}(\alpha,\beta,\gamma)\left|+\frac{1}{2}\right\rangle + c_{-\frac{1}{2}f}(\alpha,\beta,\gamma)\left|-\frac{1}{2}\right\rangle \quad [16]$$

$$\left|\phi_g^{\mathrm{X}}(\alpha,\beta,\gamma)\right\rangle = c_{+1,g}(\alpha,\beta,\gamma)|+1\rangle + c_{0,g}(\alpha,\beta,\gamma)|0\rangle + c_{-1,g}(\alpha,\beta,\gamma)|-1\rangle. \quad [17]$$

The six eigenfunctions of the combined AX spin system are then constructed from the products of the A and X eigenfunctions:

$$\left|\psi_{f,g}^{\mathrm{o}}(\alpha,\beta,\gamma)\right\rangle = \left|\phi_f^{\mathrm{A}}(\alpha,\beta,\gamma)\right\rangle \times \left|\phi_g^{\mathrm{X}}(\alpha,\beta,\gamma)\right\rangle. \quad [18]$$

The change in energy due to the chemical shift and the coupling is obtained by applying the AX wavefunction to the first-order perturbation Hamiltonian $\hat{H}_{\mathrm{AX}}^{\mathrm{pert}}$:

$$\Delta E_{f,g}^{\mathrm{pert}}(\alpha,\beta,\gamma) = \left\langle\psi_{f,g}^{\mathrm{o}}(\alpha,\beta,\gamma)\right|\hat{H}_{\mathrm{AX}}^{\mathrm{pert}}(\alpha,\beta,\gamma)\left|\psi_{f,g}^{\mathrm{o}}(\alpha,\beta,\gamma)\right\rangle. \quad [19]$$

Assuming the adiabatic approximation (the sample rotation does not change the coherence between the carbon eigenstates and each nitrogen nucleus remains in one of its eigenstates), the three observed frequencies, one for each spin-1 state labeled with g, in the rotating frame for spin A relative to the reference frequency is then simply

$$\omega_g(\alpha,\beta,\gamma) = \frac{1}{\hbar}\left(\Delta E_{1,g}^{\mathrm{pert}}(\alpha,\beta,\gamma) - \Delta E_{2,g}^{\mathrm{pert}}(\alpha,\beta,\gamma)\right). \quad [20]$$

The expansion coefficients $W_{g,m}$ for each spin-1 state are then obtained with

$$W_{g,m}(\alpha,\beta) = \frac{1}{2\pi}\int_0^{2\pi} d\gamma\, \omega_g(\alpha,\beta,\gamma)e^{-im\gamma}. \quad [21]$$

The complete FID for one spin A consists of a superposition of three FIDs, one for each state g. Each FID must be calculated separately using the corresponding $W_{g,m}(\alpha,\beta)$.

This method may easily be extended to other AX systems such as A = ^{15}N, ^{29}Si, ^{31}P, and ^{19}F, and X = ^{2}H, ^{35,37}Cl, and ^{27}Al by accommodating the four states of the spin-3/2 ^{25,37}Cl nuclei or the six states of the spin-5/2 ^{27}Al in the X spin space.

EXPERIMENTAL

Natural abundance ^{13}C and ^{14}N α-glycine, *l*-alanine, *l*-asparagine monohydrate, and *l*-histidine monohydrate monochloride were obtained from Sigma–Aldrich and used without further purification. The γ form of glycine was obtained from recrystallization of glycine from a methanol/water solution. All samples were microcrystalline and ground to fine white powders. The narrow linewidth (15–25 Hz) of the uncoupled resonance lines confirms the crystallinity of the samples. The polymorphic purity of α- and γ-glycine is confirmed by comparison to the reported ^{13}C isotropic chemical shifts and ^{1}H T_1 (*27*). In addition the conformation of all investigated compounds is confirmed by comparison to accurate *ab initio* calculations on the known single-crystal structures (*28*).

High-speed MAS and FIREMAT experiments were performed on a CMX200 (4.7 T) and a CMX400 (9.4 T) spectrometer operating at carbon frequencies of 50.305 and 100.621 MHz, respectively. Both spectrometers are equipped with 7.5-mm PENCIL probes with a feedback circuit to synchronize the pulse sequence to the rotor position. In all experiments transverse magnetization was produced by cross polarization from protons. The π pulses for protons and carbons were approximately 8 μs for all experiments on both spectrometer systems. TPPM (*29, 30*) decoupling was used with a phase shift angle of 16° and 36° for the high-speed CPMAS and FIREMAT experiments, respectively. The spinning speed for the FIREMAT experiments was $\omega_r = 2\pi \cdot 500$ Hz at both fields. At 50.305 MHz 16 evolution increments and at 100.621 MHz 32 increments were taken for all compounds; the spectral widths in the acquisition dimension were 48 and 96 kHz and in the evolution dimension they were 8 and 16 kHz, respectively. All spectra were referenced externally to the TMS shift scale by the downfield resonance of adamantane at 38.56 ppm. The sidebands in the high-speed CPMAS experiments were suppressed using the TOSS sequence (*31*). The proton T_1 values were determined using the saturation recovery method.

The FIREMAT FID was calculated numerically using Eq. [5] by software written in Fortran77. The angular frequency $\omega_g(\alpha,\beta,\gamma)$ for 16 evenly spaced positions around a cone at the magic angle to the spinner axis (see Fig. 2) is calculated as described above. The expansion coefficients $W_{g,m}$ are then obtained by a numerical fast Fourier transformation of these 16 frequencies. Investigating numerically the size of the expansion coefficients $W_{g,m}(\alpha,\beta)$ at the lowest field 4.7 T and a quadrupolar coupling constant of 4 MHz reveals that in this case the expansion coefficients $W_{g,m}(\alpha,\beta)$ with $|m| > 4$ are small and may be neglected in the banded matrix. The sideband intensities $A_{g,k}(\alpha,\beta)$ were evaluated from the expansion coefficients $W_{g,m}(\alpha,\beta)$ with $|m| \leq 4$ using the banded matrix approach (*14*) POWDER (*32*) was used with $N = 16$ to generate 513 spinner axis orientations on one hemisphere and to interpolate the FIDs. Thus, $\omega_g(\alpha,\beta,\gamma)$ was calculated for 8208 different $\mathbf{B}_o$ orientations. The resulting complex 2D FID was then fit to the experimental complex FIREMAT FID by nonlinear least-squares fitting using a SIMPLEX algorithm (*33*).

The experimental data for all compounds were initially processed using TIGER (*11*) only for the purpose of obtaining good starting values for the fitting procedure using the full theory on

TABLE 1
Quadrupolar Coupling Tensors

		χ/MHZ	η_{EFG}	$\theta/^\circ$	$\phi/^\circ$
α-Glycine[a]		1.18	0.54	7	28
γ-Glycine[b]		1.15	0.40	0	0
l-Alanine[c]		1.21	0.26	0	0
l-Asparagine[d]	N1	1.15	0.22	3	40
	N2	−2.68	0.33	89	6
l-Histidine[e]	N1	1.15	0.19	3	0
	N2	1.47	0.27	33	0
	N3	−1.29	0.95	90	126

Note. The quadrupolar coupling tensors are taken from: [a]Ref. (*39*); [b]the quadrupolar coupling tensor for γ-glycine is an estimate based on the values found for the other amino acids; [c]Ref. (*40*); [d]Ref. (*41*); [e]Ref. (*42*).

the complete FIREMAT FID as outlined above. Considering all interactions encountered in this problem, 13 variable parameters are required to fully characterize the sideband pattern. When the known quadrupolar tensor values given by χ and η_{EFG} and the internuclear vector defined by θ and ϕ are used, this is reduced to 9 remaining parameters. These fitted parameters are $\delta_{11}, \delta_{22}, \delta_{33}$, $\Re(\iota, \kappa, \lambda)$, the dipolar coupling constant D, and Gaussian and Lorentzian line broadening. One avoids fitting the quadrupolar coupling tensor because it is not well determined by the data and correlation with other fitting parameters may introduce bias to the results obtained for the more important shift and dipolar parameters (see below). The quadrupolar coupling constants and asymmetries for all compounds are given in Table 1. For γ-glycine, approximations were based on the values for α-glycine and *l*-alanine, since NQR data are not available.

RESULTS AND DISCUSSION

Sensitivity of sideband spectra to ^{13}C–^{14}N dipolar coupling. In order to show the sensitivity of the spinning sideband manifold to the attributes of the ^{13}C–^{14}N dipolar coupling, several simulations at both 4.7 and 9.4 T with varying parameters are compared in Figs. 4a through 4j. The difference plots of the simulations with varying parameters with respect to the central simulation which is shown at the bottom of each figure reveal that the sideband manifold is sensitive to both the dipolar coupling constant D and the orientation of the chemical shift principal axes at both fields. Only the rotation of the chemical shift tensor around the internuclear vector fails to produce significant spectral effects, presumably because of the axial symmetry of the dipolar interaction that is only weakly broken by the quadrupolar coupling. When the residue values at the two fields are compared it is apparent that the spectra at 4.7 T are two to three times more sensitive to changes in orientation and D. In order to assess the significance of the residues obtained by changing the dipolar and orientational parameters, several simulations performed with varying shift principal values at both 9.4 and 4.7 T are shown in Figs. 4e and 4j. The differences in principal values for these simulations are in the range of typical accuracies from sideband fitting. The relative residues with respect to the signal intensity for changes in the principal values have magnitudes similar to the ones resulting from changes in D and in the orientation of the principal axes. This clearly shows that the orientational and ^{13}C–^{14}N dipolar information may be extracted from the ^{13}C sideband manifolds, when the signal-to-noise is adequate and when a sufficient number of sidebands is present, as discussed by Hodgkinson and Emsley (*34*).

Amino Acid Experiments

For the following discussion the numbering shown in Scheme 1 is used.

FIREMAT spectra. The FIREMAT absolute value spectrum recorded at 4.7 T for *l*-histidine is shown in Fig. 5a. The best fit of this spectrum in Fig. 5d shows excellent agreement with the experimental data. The full expansion of the C1 sideband manifold in Figs. 5b, 5c and 5e, 5f demonstrates that all features of the dipolar-coupled sidebands are well described. The small deviations between theory and experiment may be due to different linewidth of spins coupled to nitrogen in different angular spin states (*35*), an effect that is neglected here to keep the number of adjustable parameters reasonable. In Figs. 5b and 5e the ^{14}N-coupled C1 2D lineshape may be compared to the uncoupled C2 lineshape. It is apparent that the coupled 2D lineshape reveals a complexity that is absent in uncoupled lines. This complexity allows for a good determination of the fitted parameters.

The recorded and best-fit FIREMAT spectra of *l*-histidine at 9.4 T appear in Fig. 6. The broadening due to the quadrupolar interaction at 9.4 T is not apparent in the lineshapes of the sidebands, and nearly symmetric lineshapes are observed. The dipolar coupling to ^{14}N, however, alters the amplitude of the sidebands and cannot be neglected in the model describing the sideband manifold.

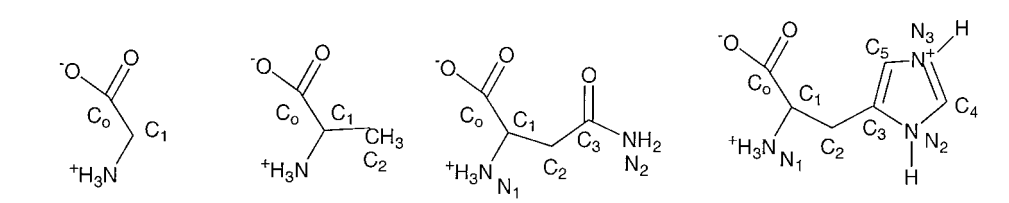

SCHEME 1

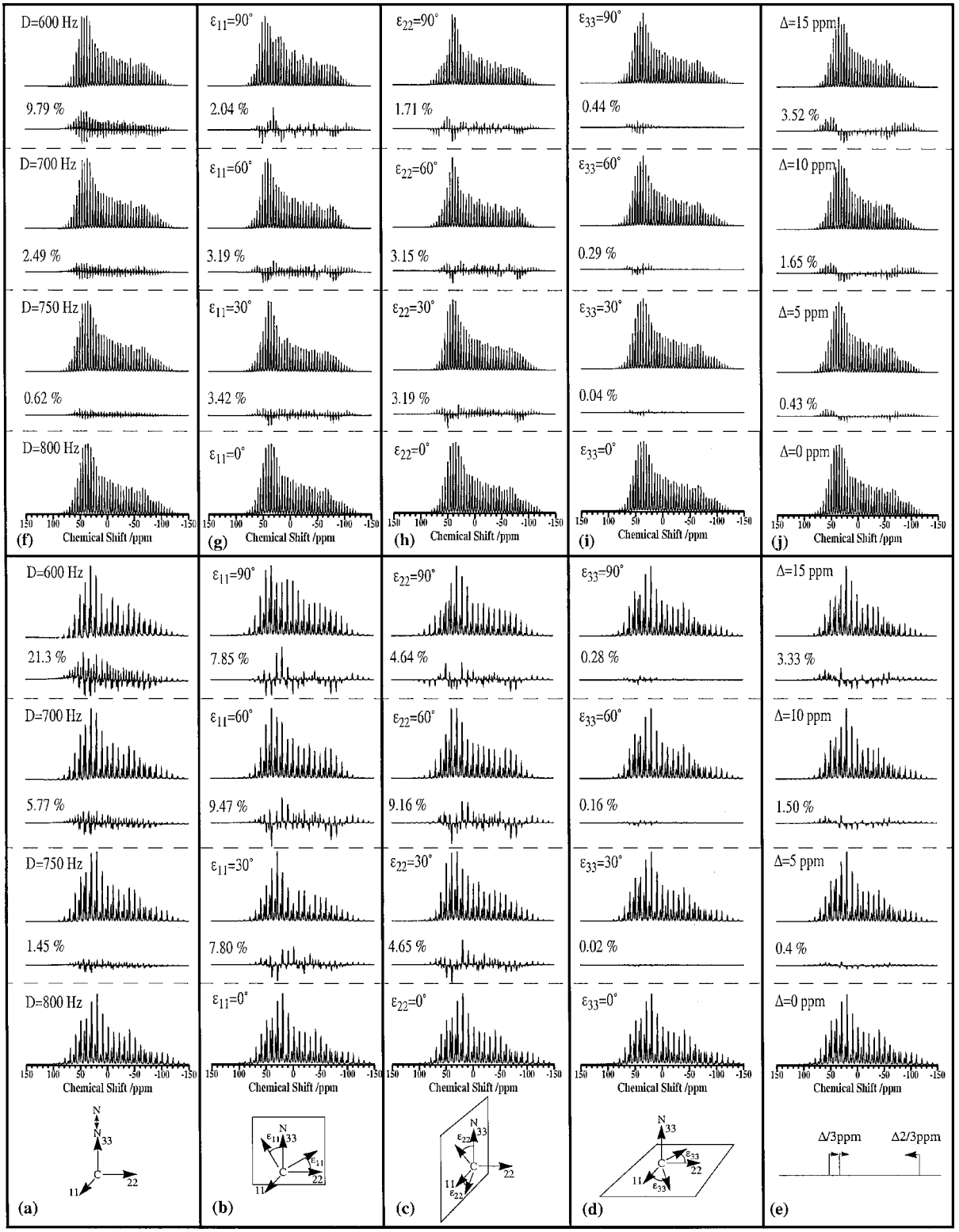

FIG. 4. Comparison of the Fourier transform of the first evolution increment of a FIREMAT FID (*48*) that results from a ^{13}C coupled to a ^{14}N, (a–e) at 4.7 T and (f–j) at 9.4 T. The following parameters are used for the central simulation at the bottom of (a–j): $\chi = 4$ MHz, $\eta_{EFG} = 0.5$, $D = 800$ Hz, $\delta_{11} = 60$ ppm, $\delta_{22} = 40$ ppm, and $\delta_{33} = -100$ ppm. The 33-axis of the shift tensor is collinear with the dipolar vector and the unique EFG principal axis. The spinning speed is $\omega_r = 2\pi \cdot 500$ Hz and 50 Hz line broadening was applied in all simulations. The parameter varied from the central simulation is given in the upper left corner of the individual simulations. The residue to the central simulation is shown below each simulation.

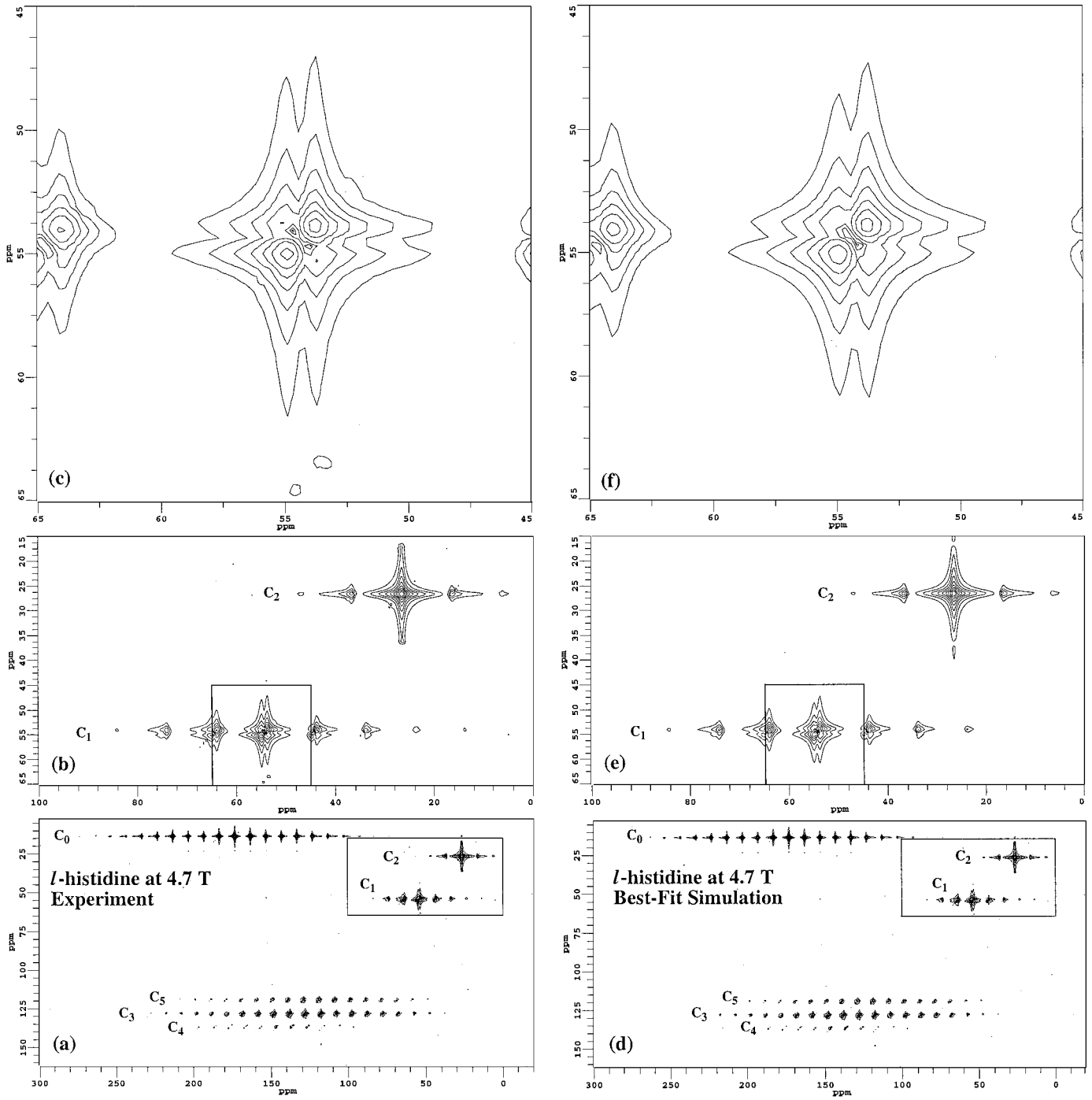

FIG. 5. Experimental and best-fit simulation FIREMAT absolute value spectra of *l*-histidine recorded at 4.7 T. The C0 sideband manifold is folded in the isotropic dimension. (a) Full experimental spectrum. (b) Expansion of C1 and C2 sideband patterns from the experimental spectrum. (c) Expansion of highest intensity C1 sideband from the experimental spectrum. (d) Full best-fit simulation. (e) Expansion of C1 and C2 sideband patterns from the best-fit simulation. (f) Expansion of highest intensity C1 sideband from the best-fit simulation.

Dependence of the fitted parameters on the assumed quadrupolar coupling. Fits were done with systematically altered quadrupolar couplings and asymmetries to investigate the influence of the quadrupolar tensor magnitudes on the dipolar coupling and shift principal values obtained. The results for the C1 resonance of α-glycine are plotted in Fig. 7. All ^{13}C–^{14}N systems investigated showed the same trends as these examples. At both fields the residue value is only weakly dependent on

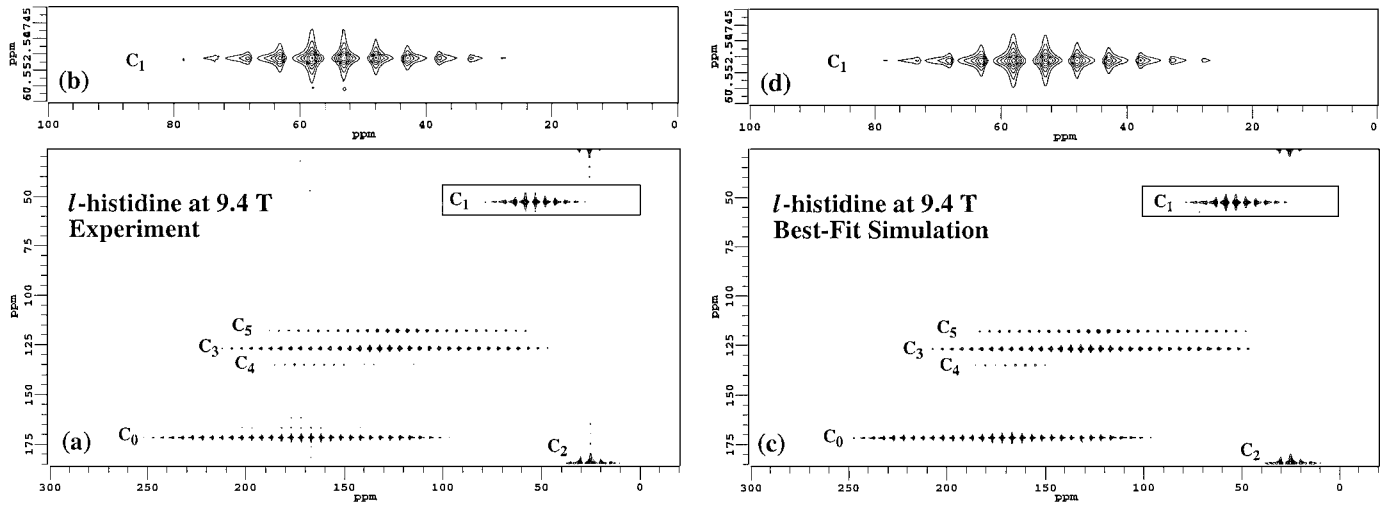

FIG. 6. Experimental and best-fit simulation FIREMAT absolute value spectra of *l*-histidine recorded at 9.4 T. The C2 sideband manifold is aliased in the isotropic dimension. (a) Full experimental spectrum. (b) Expansion of C1 sideband pattern from the experimental spectrum. (c) Full best-fit simulation. (d) Expansion of C1 sideband pattern from the best-fit simulation.

the quadrupolar coupling when the dipolar and chemical shift parameters are optimized by the SIMPLEX routine. The minimum of the residue value for C1 with respect to the quadrupolar coupling constant χ is at about $\chi = 1.1$–1.2 MHz at both fields. This is in agreement with the value found from single-crystal ^{14}N NMR of $\chi = 1.18$ MHz. However, extracting χ from the 2D datasets is aggravated by a large correlation between D and χ. Other specialized methods are available to obtain more reliable χ.

It can be seen from Fig. 7 that D obtained from the fitting is strongly dependent on the assumed value of χ. This may be explained with the fact that the lineshape of the sidebands contributes significantly to the information content of the spectrum

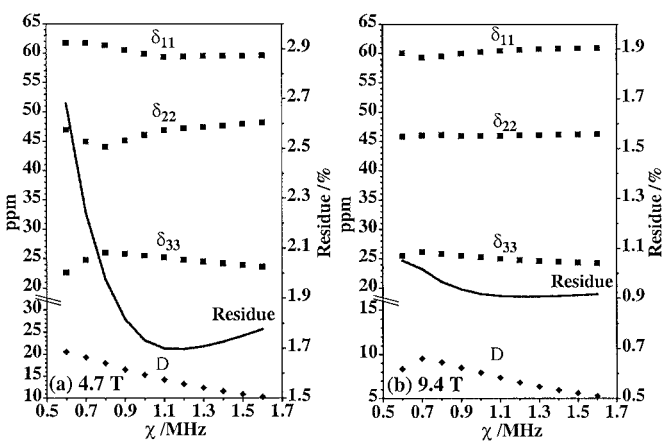

FIG. 7. Correlation of the principal shift values and the dipolar coupling constant D with the quadrupolar coupling constant for the C1 resonance of α-glycine. The residue values represent the fit of both carbon positions of α-glycine.

and lineshape discrepancies between model and data result in increased residues. The 2 : 1 doublet lineshape, however, depends approximately on the product of χ and D, as may be seen from the relation derived by Olivieri *et al.* (*36*) and Gan and Grant (*20*) for the splitting of the 2 : 1 doublet under MAS conditions

$$S = \frac{9}{20}\frac{D\cdot\chi}{\omega_{14N}}(3\cos^2\theta - 1 + \eta_{EFG}\sin^2\theta\cos 2\phi), \qquad [22]$$

where ω_{14N} is the ^{14}N Larmor frequency. Thus an underestimated D results from fitting with an assumed value of χ that is too large, and vice versa. This dependence is not expected at 9.4 T where in most cases only slightly distorted lineshapes are observed. The linewidth, however, is still sensitive to the broadening due to the dipolar coupling and in addition the complicated sideband intensities are affected by the ^{13}C–^{14}N dipolar coupling.

From Eq. [22] it is also evident that the correlation of the asymmetry η_{EFG} of the quadrupolar coupling with the dipolar coupling constant depends on the orientation of the dipolar tensor relative to the principal axes of the EFG tensor, when the same lineshape arguments are used. As θ approaches 0° the fits become less dependent on η_{EFG}. This situation is encountered for all C1 carbons where θ is small.

In Fig. 7 the chemical shift principal values obtained from the fits are less correlated to χ than is D. In addition the shifts are less dependent on the quadrupolar coupling at higher field, as expected. At 9.4 T the changes in the chemical shift principal values are generally within 1 ppm and at 4.7 T within about 3 ppm when χ is varied by 1 MHz. Therefore, it is apparent that including the quadrupolar coupling among the fitted parameters is not feasible. The quadrupolar coupling is better thought of as a perturbation that must be considered in the analysis in order to obtain improved principal shift values and dipolar coupling

constants. The consequences of the quadrupolar coupling are important for further applications of this method, since many quadrupolar coupling tensors have not been measured and must be estimated in order to extract the shift and dipolar parameters. It should be noted that a greater impact upon the shift tensor may be encountered in other compounds with larger quadrupolar and dipolar coupling constants.

Chemical shift principal values. The chemical shift principal values for the coupled resonances of α-glycine, *l*-alanine, and *l*-asparagine extracted using the full theory on the FIREMAT datasets are compared with the corresponding values obtained by single-crystal NMR in Table 2. The values at 9.4 T are in excellent agreement with the single-crystal data. The standard deviation in the coupled shifts, those of carbons bonded to nitrogen, is 2.4 ppm, comparable to the accuracy for the uncoupled carbons. Essentially the same standard deviation of 2.6 ppm for the coupled resonances is obtained at 4.7 T when the full theory is used. However, the insensitivity of the principal shift values relative to variations in the assumed quadrupolar coupling and the accuracy of the shift values at 9.4 T favors the collection of the experimental data at higher field, when accurate quadrupolar coupling data are not available.

TIGER processing of the 9.4 T FIREMAT data and fitting the extracted sideband pattern with a chemical shift sideband model results in a standard deviation of 4.4 ppm for the coupled carbons. This is somewhat higher than the precision achieved for the analysis of sideband manifolds resulting from carbons without ^{14}N couplings. It is also apparent from the larger and systematic residues that a less than adequate model has been applied. However, these approximate principal shift values provide a convenient starting point for fitting the FIREMAT FID with the full theory.

TABLE 2
Shift Principal Values for the ^{13}C–^{14}N Coupled Resonances

		δ_{11}/ppm	δ_{22}/ppm	δ_{35}/ppm
α-Glycine	SC[a]	65.7	45.1	26.3
	9.4 T	60.3	46.0	24.8
	4.7 T	59.3	47.2	24.9
l-Alanine	SC[b]	64.6	56.0	30.8
	9.4 T	66.0	55.2	32.3
	4.7 T	65.6	56.5	31.2
l-Asparagine C1	SC[c]	71.3	53.0	29.6
	9.4 T	68.5	53.3	31.3
	4.7 T	69.0	53.5	30.6
l-Asparagine C3	SC[c]	245.7	196.1	88.0
	9.4 T	246.2	196.7	84.0
	4.7 T	247.2	194.9	84.6
γ-Glycine	9.4 T	59.2	44.5	20.6
	4.7 T	58.2	48.1	21.8
l-Histidine C1	9.4 T	68.5	57.0	37.8
	4.7 T	72.9	58.6	31.4
l-Histidine C3	9.4 T	202.7	132.3	49.8
	4.7 T	203.3	131.5	50.0
l-Histidine C5	9.4 T	190.9	122.8	44.3
	4.7 T	193.0	122.3	44.6
Standard deviation	9.4 T	2.4 ppm		
to SC	4.7 T	2.6 ppm		

Note. SC, Single-crystal NMR data; 4.7 T, FIREMAT at 4.7 T; 9.4 T, FIREMAT at 9.4 T. Principal shift values taken from: [a]Ref. (*39*); [b]Ref. (*40*); [c]Ref. (*41*).

TABLE 3
Dipolar Coupling Constants

		Neutron diffraction		FIREMAT at 4.7 T		FIREMAT at 9.4 T	
		r C–N/Å	D/Hz	D/Hz	r C–N/Å	D/Hz	r C–N/Å
α-Glycine[a]		1.476	680	676	1.48	696	1.46
γ-Glycine[b]		1.461	701	685	1.47	751	1.43
l-Alanine[c]		1.486	666	630	1.51	609	1.53
l-Asparagine[d]	C1–N1	1.490	661	659	1.49	664	1.49
l-Asparagine[d]	C3–N2	1.332	924	896	1.35	1027	1.29
l-Histidine[e]	C1–N1	1.485	666	661	1.49	655	1.49
l-Histidine[e]	C3–N2	1.383	826	791	1.40	768	1.42
l-Histidine[e]	C5–N3	1.375	840	818	1.39	828	1.38

Note. Neutron diffraction data taken from: [a]Ref. (*43*); [b]Ref. (*44*); [c]Ref. (*45*); [d]Ref. (*46*); [e]Ref. (*47*).

Dipolar coupling. The dipolar coupling constants obtained from fitting the FIREMAT FIDs are given in Table 3 along with the expected ones calculated from the neutron diffraction data and the respective bondlengths; the correlation is shown in Fig. 8. The standard deviation of the dipolar coupling constants is 24 Hz for the data recorded at 4.7 T and 50 Hz for the data recorded at 9.4 T. At 4.7 T a distinct 2 : 1 doublet is observed in the experimental data and the dipolar coupling determines not only the

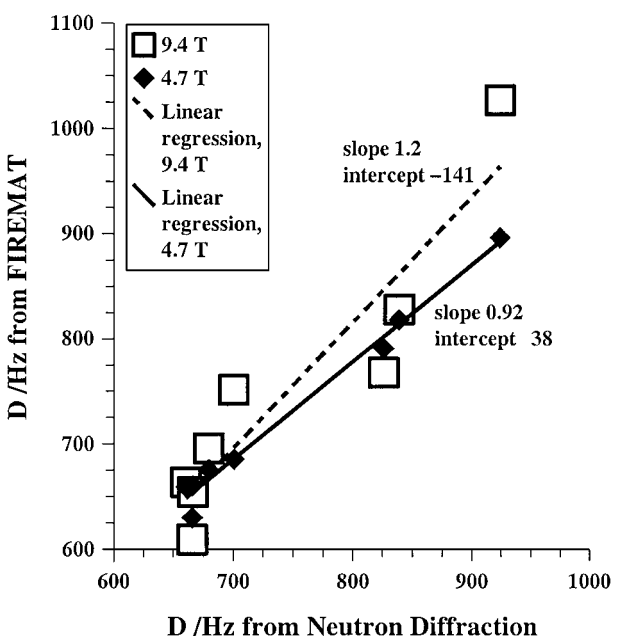

FIG. 8. Correlation plot of D determined from the FIREMAT FIDs at 4.7 and 9.4 T with D calculated from neutron diffraction structures.

sideband intensities but also each sidebands' lineshape. At 9.4 T D is primarily determined by the sideband intensities, as only a small lineshape perturbation is noted from the quadrupole interaction. This results in reduced sensitivity to D and less accuracy at 9.4 T. This sensitivity on D is also observed in the simulations of Figs. 4a and 4f where the residual values for changes in D are about twice as large at 4.7 T than at 9.4 T. Since D is highly correlated with the quadrupolar coupling constant χ at both fields, see Fig. 7, it is important to have an accurate quadrupolar coupling tensor available when reliable dipolar coupling constants are needed at both fields.

Orientation of the dipolar tensor in the shift principal axis system. The orientational information extracted from the FIREMAT FIDs and the single-crystal results are shown in Table 4 for comparison; the angles used are explained in Fig. 9. In dipolar-coupled systems involving two spin-1/2 nuclei only partial information on the orientation of the shift principal axes in the molecular frame may be extracted from powdered solids. This limitation of dipolar spectroscopy results from the axially symmetric dipolar tensor in the chemical shift PAS. The axial symmetry of the dipolar tensor is broken by the quadrupolar interaction at the ^{14}N nucleus, and the complete shift tensor including the orientation may in principle be extracted from the sideband spectrum, provided that the EFG tensor is known. However, due to the small quadrupolar interaction at the ^{14}N and the small dipolar coupling constant for ^{13}C–^{14}N, the sideband manifold exhibits only minor effects on rotation of the CSA around the unique dipolar axis, as shown in Figs. 4d and 4i. Hence, only two of three shift tensor orientational angles may be retrieved from the sideband spectra.

TABLE 4
Orientation of the Dipolar Tensor in the Shift Principal Axis System

		∠11	∠22	∠33	∠SC/FIREMAT
α-Glycine[a]	SC	77.7	54.7	38.0	
	9.4 T	82.0	56.8	34.4	5.0
	4.7 T	82.2	60.6	30.7	7.8
l-Alanine[b]	SC	82.8	65.7	25.5	
	9.4 T	81.2	63.6	28.1	2.8
	4.7 T	71.8	75.3	23.7	14.1
l-Asparagine[c] C1–N1	SC	83.1	64.7	26.3	
	9.4 T	79.2	59.5	32.7	6.7
	4.7 T	81.3	63.0	28.6	2.6
l-Asparagine[c] C3–N2	SC	40.7	49.3	89.7	
	9.4 T	43.5	46.5	89.3[d]	2.9
	4.7 T	43.5	46.5	89.3[d]	2.9
γ-Glycine	9.4 T	87.4	60.1	30.1	
	4.7 T	83.7	65.2	25.7	
l-Histidine C1–N1	9.4 T	72.9	63.8	32.0	
	4.7 T	67.6	71.3	29.5	
l-Histidine C3–N2	9.4 T	19.2	70.8	90.0[d]	
	4.7 T	19.4	70.6	90.0[d]	
l-Histidine C5–N3	9.4 T	25.5	64.5	90.0[d]	
	4.7 T	23.4	66.6	90.0[d]	
Average angle	9.4 T				4.3
to C–N_{SC}	4.7 T				6.8

Note. SC, Single-crystal NMR data; 4.7 T, FIREMAT at 4.7 T; 9.4 T, FIREMAT at 9.4 T. Orientations taken from: [a]Ref. (*39*); [b]Ref. (*40*); [c]Ref. (*41*); [d]the angle was not optimized because of the local symmetry at the carbon position.

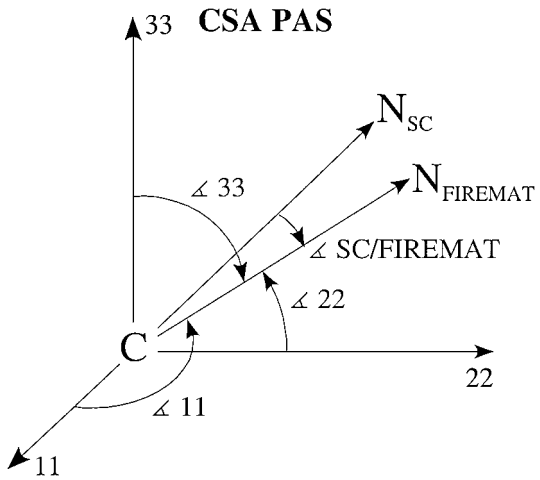

FIG. 9. Description of the dipolar vector orientation in the shift principal axis system.

When the local symmetry of the molecule requires a unique orientation of one of the shift principal values, the complete orientational information of the shift tensor may be found. This is the case for the shift tensors of C3 in *l*-asparagine and C3 and C5 in *l*-histidine, where the δ_{33} shift principal value can be assumed to be perpendicular to the local planar geometry. The orientations of the C3 and C5 shift principal axes within the molecular frame are shown in Fig. 10, since they are not known from single-crystal results. In order to allow comparison between single-crystal data and FIREMAT results the orientation of the unique axis of the dipolar tensor (i.e., the **CN** bond vector) within the shift principal axis system for all ^{13}C–^{14}N systems is compared. The results are shown in Table 4. The

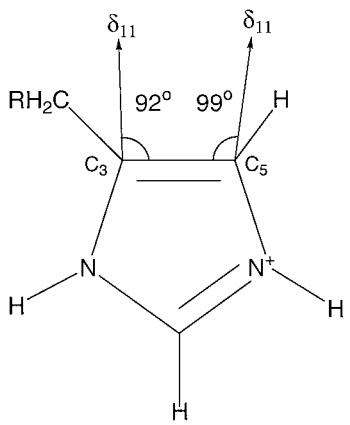

FIG. 10. Orientation of the principal shift values for C5 and C3 of *l*-histidine relative to the molecular frame. Only δ_{11} is shown, since δ_{33} is perpendicular to the aromatic plane. The orientation of δ_{22} follows from the orthogonality.

average angle between the **CN** vector obtained from fitting the FIREMAT FID ($\mathbf{CN}_{\mathrm{FIREMAT}}$) and the **CN** vector from single-crystal data ($\mathbf{CN}_{\mathrm{SC}}$) is about 5° for the 9.4 T data and 7° for the 4.7 T data. These deviations may be compared to those obtained by separated local field experiments and GIAO *ab initio* methods in which standard deviations of about 5° are observed. (*37*) As for the dipolar coupling, the effect of the number of sidebands present in the spectrum on the uncertainty of the orientation is not addressed. The method described here has an accuracy that is suitable for determining orientational information on the shift principal values without the need for a more elaborate experiment. This additional orientational information provides a more detailed discussion of electronic effects and better comparison between experiment and *ab initio* methods.

CONCLUSIONS

The effects of dipolar coupling in ^{13}C–^{14}N systems on ^{13}C FIREMAT experiments can be accommodated with an accurate theoretical model. Fitting this model to the FIREMAT FID extracts chemical shift principal values and dipolar tensor information with good accuracy when the quadrupolar tensor is known. The chemical shift principal values obtained from the fits are less dependent, as is well known, on the assumed quadrupolar coupling at higher field. Accurate dipolar tensors may be found at either field only when the exact quadrupolar coupling tensor is available because of high correlation between these two interactions at either field strength.

APPENDIX

Isotropic/anisotropic separation in $(2N-1)\pi$ experiments. The pulse sequences for a general $(2N-1)\pi$ experiment where N is an integer and the commonly used 5π pulse sequence of the FIREMAT experiment where N is 3 are shown in Fig. a. The initial transverse magnetization M_o is created at $t=0$ using cross polarization from protons. Then during one rotor period of duration $T=2\pi/\omega_r$, π pulses are applied, in N cycles consisting of two pulses each. The first π pulse in the first cycle is replaced with the cross polarization. The pulses are applied at times

$$\tau_j = j\frac{T}{2N} - \frac{t_1}{2N} \quad \text{for even } j$$

$$\tau_j = j\frac{T}{2N} \quad \text{for odd } j,$$

where t_1 is the evolution time and j goes from 1 to $2N$. The acquisition is started at $t=T$.

The FID for this slow spinning 2D $(2N-1)\pi$ MAT experiment for a single crystallite may be written as (*11*)

$$\rho_{2D}(\alpha,\beta,\gamma \mid t_1,t_2) = \exp[-i\Phi(\alpha,\beta,\gamma \mid t_1)] \cdot \sum_k a_k(\alpha,\beta,\gamma) \cdot \exp[-i(W_o(\alpha,\beta)+k\omega_r)t_2], \quad [a]$$

where t_2 is the detection time. The α,β,γ powder angles relate the crystallite reference frame to the lab frame at $t=0$. The $\sum_k a_k(\alpha,\beta,\gamma)\cdot\exp[-i(W_0(\alpha,\beta)+k\omega_r)t_2]$ detection-dimension term represents the FID of a rotating crystallite. The term $\exp[i\Phi(\alpha,\beta,\gamma \mid t_1)]$ represents the evolution of the magnetization during the rotor period occupied by the $(2N-1)\pi$ pulses. The net phase angle $\Phi(\alpha,\beta,\gamma \mid t_1)$ accumulated during the rotor period may be expressed by the sum of the $2N$ individual phase angles $\Phi_j(\alpha,\beta,\gamma \mid t_1)$ that accumulate between the π pulses. Since a π pulse reverses the sign of the accumulated phase, the total phase angle is given by

$$\Phi(\alpha,\beta,\gamma \mid t_1) = \sum_{j=1}^{2N}(-1)^j \Phi_j(\alpha,\beta,\gamma \mid t_1). \quad [b]$$

The individual phase angles $\Phi_j(\alpha,\beta,\gamma \mid t_1)$ may be expressed as integrals of the Larmor frequency $\omega(\alpha,\beta,\mid\gamma)$:

$$\Phi_j(\alpha,\beta,\gamma \mid t_1) = \int_{t_a}^{t_b} \omega(\alpha,\beta,\gamma \mid t)\,dt. \quad [c]$$

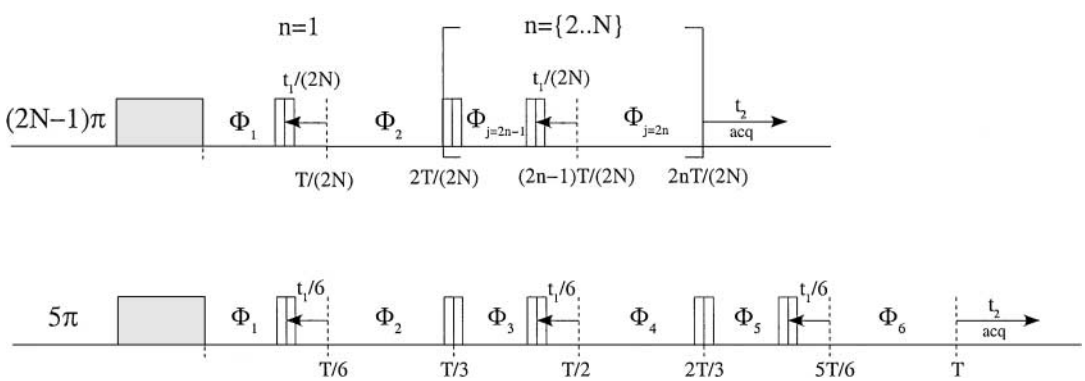

FIG. a. X channel $(2N-1)\pi$ pulse sequence and 5π pulse sequence of the FIREMAT experiment.

The limits t_a and t_b are defined by the times the π pulses are applied to reverse the phase:

	Odd j	Even j	
t_a	$\frac{(j-1)}{2N}\cdot T$	$\frac{(j-1)}{2N}\cdot T-\frac{t_1}{2N}$	[d]
t_b	$\frac{j}{2N}\cdot T-\frac{t_1}{2N}$	$\frac{j}{2N}\cdot T$	

The Larmor frequency $\omega(\alpha,\beta,\gamma\,|\,t)$ depends on the orientation of each crystallite relative to the external magnetic field $\mathbf{B}_o$. When the sample is rotated around the rotor axis **S** with angular frequency ω_r, $\mathbf{B}_o$ and thus the Larmor frequency ω become time dependent. Figure b shows the mechanical rotation in the EFG PAS. Because of the periodicity of $\omega(\alpha,\beta,\gamma\,|\,t)$ in the angle γ, it may be conveniently expanded in a Fourier series as has been employed previously (*38, 14*). Since the powder angle γ and the mechanical rotation $\omega_r\cdot t$ describe rotations around the same axis, the time dependence of $\omega(\alpha,\beta,\gamma\,|\,t)$ may be expressed as

$$\omega(\alpha,\beta,\gamma\,|\,t)=\sum_{m=-\infty}^{\infty}W_m(\alpha,\beta)\exp[im\gamma]\cdot\exp[im\omega_r\cdot t]. \quad [e]$$

Explicit expansion coefficients may easily be obtained, analytically for the most common interactions or numerically in complicated cases (*14*).

Substituting the Fourier expansion for $\omega(\alpha,\beta,\gamma\,|\,t)$ into Eq. [c] yields integrals of the form

$$\Phi_j(\alpha,\beta,\gamma\,|\,t_1)=\sum_{m=-\infty}^{\infty}W_m(\alpha,\beta)\cdot\exp[im\gamma]\int_{t_a}^{t_b}\exp[im\omega_r t]\,dt. \quad [f]$$

Solving these integrals and substituting the results into Eq. [b], combining the sums over odd and even j, collecting terms, and combining W_m and W_{-m} for terms with $m=\pm p\cdot N$ yield for the phase angle accumulated by the $(2N-1)\pi$ pulses at the start of the acquisition

$$\Phi(\alpha,\beta,\gamma\,|\,t_1)=W_0(\alpha,\beta)\cdot t_1+\sum_{m=1}^{\infty}\Theta_m(\alpha,\beta,\gamma\,|\,t_1). \quad [g]$$

$\Theta_m(\alpha,\beta,\gamma\,|\,t_1)$ is the accumulated phase angle due to the corresponding W_m term. When m is not an integer multiple of the sequence number N, $\Theta_m(\alpha,\beta,\gamma\,|\,t_1)$ vanishes; if m is a nonzero integer multiple of N it becomes

$$\Theta_m(\alpha,\beta,\gamma\,|\,t_1)=\frac{4N}{m\omega_r}[\mathrm{Re}(W_m(\alpha,\beta))\cdot A+\mathrm{Im}(W_m(\alpha,\beta))\cdot B], \quad [h]$$

where $m=p\cdot N$ and $p=\{1,2,\ldots,\infty\}$. The factors A and B are

$$A=\sin p\gamma+(-1)^p\sin\left(\frac{p\omega_r t_1}{2}-p\gamma\right)$$

$$B=\cos p\gamma-(-1)^p\cos\left(\frac{p\omega_r t_1}{2}+p\gamma\right).$$

Thus the sum over m in Eq. [g] may be replaced with a sum over p and the net phase accumulation may be expressed as

$$\Phi(\alpha,\beta\,|\,t_1)=W_0(\alpha,\beta)\cdot t_1+\sum_{p=1}^{\infty}\Theta_{pN}(\alpha,\beta,\gamma\,|\,t_1). \quad [i]$$

The term $W_0(\alpha,\beta)\cdot t_1$ represents the intended function of the pulse sequence, to encode the isotropic frequency. The sum represents any imperfections in that encoding. Substituting Eq. [i] in Eq. [a] yields for the FID of one crystallite

$$\rho_{2D}(\alpha,\beta,\gamma\,|\,t_1,t_2)=\exp\left[-i\left(W_0(\alpha,\beta)\cdot t_1+\sum_{p=1}^{\infty}\Theta_{pN}(\alpha,\beta,\gamma\,|\,t_1)\right)\right]\cdot\sum_k a_k(\alpha,\beta,\gamma)\cdot\exp[-i(W_0(\alpha,\beta)+k\omega_r)t_2]. \quad [j]$$

Integrating over the γ angle yields the magnetization μ_{2D} for the set of crystallites with common α and β angles.

$$\mu_{2D}(\alpha,\beta|t_1,t_2)=\int_0^{2\pi}d\gamma\exp\left[-i\left(W_0(\alpha,\beta)\cdot t_1+\sum_{p=1}^{\infty}\Theta_{pN}(\alpha,\beta,\gamma\,|\,t_1)\right)\right]\cdot\sum_k a_k(\alpha,\beta,\gamma)\cdot\exp[-i(W_0(\alpha,\beta)+k\omega_r)t_2]. \quad [k]$$

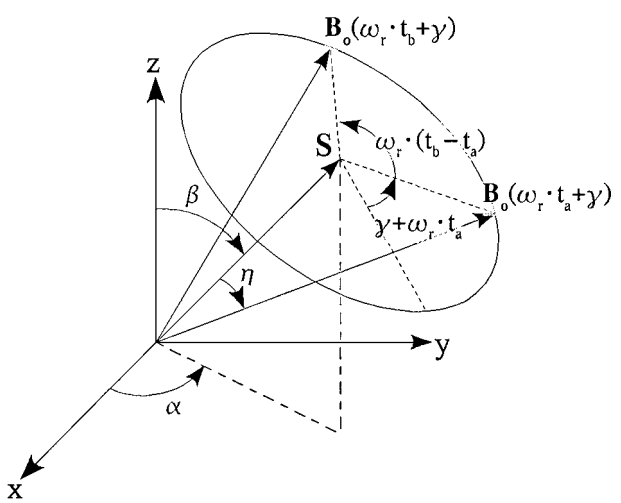

FIG. b. Description of the mechanical sample rotation that defines the time-dependent field direction $\mathbf{B}_o$ in the EFG PAS. η is the magic angle.

As it is apparent from Eq. [i] terms with $m \neq p \cdot N$ do not contribute to the phase encoding of the $(2N-1)\pi$ sequence. Only terms with $m = 0$ and $m = p \cdot N$ result in a nonvanishing phase angle and affect the observed spectrum, where the phase angle accumulated due to the term with $m = 0$ results in the isotropic spectrum. Further examination of the A and B terms in Eq. [h] reveal that the phase angle accumulated due to the W_m terms with $m = p \cdot N$, Θ_{pN}, is scaled by ω_r and periodic with an angular frequency of $p \cdot \omega_r/2$. In order to explore the effects of the higher order expansion coefficients W_{pN} on the I/A separation, the evolution dimension with $t_2 = 0$ of $\mu_{2D}(\alpha, \beta \mid t_1, t_2)$ is simulated by assuming different magnitudes for $W_{pN}(\alpha, \beta)$. The Fourier transform of $\mu_{2D}(\alpha, \beta \mid t_1, 0)$ gives the isotropic spectrum shown in Fig. c. The periodicity of the phase angle $\Theta(\alpha, \beta, \gamma \mid t_1)$ results in sidebands at $p \cdot \omega_r/2$ in this spectrum, i.e., an incomplete I/A separation.

However, the W_{p3} terms ($N = 3$ for the FIREMAT experiment) in ^{13}C–^{14}N systems are generally small compared to the spinning speed. Thus, their effect on the isotropic phase encoding is negligible in the FIREMAT experiment at sufficient high spinning speeds. This may be verified experimentally by comparing the evolution dimension with $t_2 = 0$ of the FIREMAT FID (P2DSS) with the high-speed MAS FID. This is done for the aromatic region of the *l*-histidine spectra at 4.7 T in Fig. 1. It is apparent that the *l*-histidine high-speed MAS and P2DSS spectra are identical and spectral features resulting from higher order W_{p3} are absent. Thus, at sufficiently high spinning speeds the phase angle $\Phi(\alpha, \beta, \gamma \mid t_1)$ accumulated by the $(2N-1)\pi$ pulses becomes $W_0(\alpha, \beta) \cdot t_1$, and consequently independent of γ. Hence, Eq. [k] may be rewritten as

$$\mu_{2D}(\alpha, \beta \mid t_1, t_2) = \exp[-i(W_0(\alpha, \beta) \cdot t_1)] \cdot \sum_k \exp[-i(W_0(\alpha, \beta) + k \cdot \omega_r)t_2] \times \frac{1}{2\pi} \int_0^{2\pi} d\gamma\, a_k(\alpha, \beta, \gamma). \quad [l]$$

Substituting the γ average of $a_k(\alpha, \beta, \gamma)$ with $A_k(\alpha, \beta)$ yields

$$\mu_{2D}(\alpha, \beta \mid t_1, t_2) = \exp[-iW_0(\alpha, \beta)t_1] \cdot \sum_k A_k(\alpha, \beta) \cdot \exp[-i(W_0(\alpha, \beta) + k \cdot \omega_r)t_2]. \quad [m]$$

In Eq. [m] the I/A separation is achieved by a combination of the number of cycles N and spinning speed ω_r. The complete 2D FID for a uniformly distributed powdered solid is obtained by integrating over the powder angles α and β and introducing terms accounting for the transverse relaxation with time constant T_2 during the evolution $\exp[-T/T_2]$ and acquisition $\exp[-t_2/T_2]$ period:

$$M_+(t_1, t_2) = \frac{M_0}{4\pi} \int_0^{2\pi} d\alpha \int_0^{\pi} \sin\beta\, d\beta \exp[-T/T_2] \cdot \exp[-iW_0(\alpha, \beta)t_1] \cdot \exp[-t_2/T_2] \cdot \sum_k A_k(\alpha, \beta) \cdot \exp[-i(W_0(\alpha, \beta) + k \cdot \omega_r)t_2]. \quad [n]$$

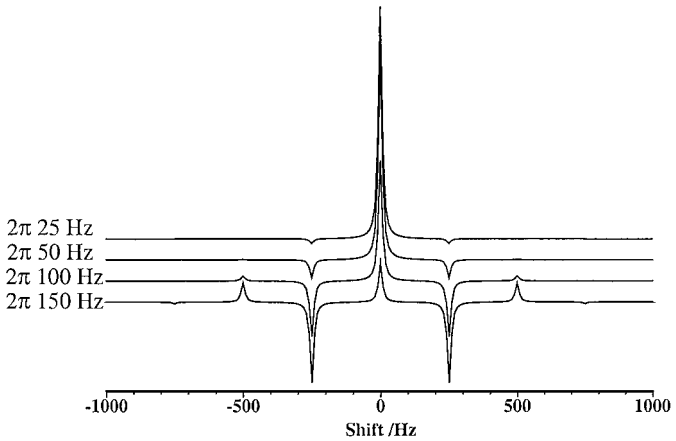

FIG. c. Simulation of the evolution dimension spectrum with $t_2 = 0$ for a 5π pulse experiment ($N = 3$). The spectra represent only the average over the "γ-carousel" for powder angles α and β. The spinning frequency is $\omega_r = 2\pi \cdot 500$ Hz; the real and imaginary parts of the expansion coefficient $W_3(\alpha, \beta)$ used for the simulation are equal and given next to the spectra.

Most commonly only interactions with rank 2 such as the chemical shift and the dipolar coupling between spin-1/2 are present in spin systems that are investigated resulting in expansions coefficients W_m with $m \leq 2$. Thus an experiment with $N = 3$ (5π experiment) is sufficient at any spinning speed to obtain the pure isotropic spectrum in the evolution dimension. However, in the case of the dipolar coupling in spin-1/2 spin ≥ 1 systems higher order W_m terms are present. Therefore, the number of cycles N and the spinning speed have to be appropriate to separate isotropic and anisotropic information.

The results derived here are general and a $(2N-1)\pi$ sequence may be used to eliminate interactions with $m \neq p \cdot N$ in the evolution dimension. Hence, a suitable number of π pulses for any spinning speed may be found to separate isotropic and anisotropic dimensions for any interaction that result in higher order expansion coefficients W_m. Figure d summarizes the terms that vanish using a $(2N-1)$ sequence. The concept of applying $(2N-1)\pi$ pulses over one rotor period may be used to set up a family of 2D solid-state experiments. In order to extend this method to higher spin quadrupolar nuclei, such as $^{35,37}Cl$ and ^{27}Al with larger quadrupolar and dipolar couplings, one must test whether the I/A separation in the FIREMAT experiment is still effective. This may be done effectively by comparing the high-speed MAS spectrum and the evolution dimension of the

$m\backslash N$	1	2	3	4	5
1	X	o	o	o	o
2	X	X	o	o	o
3	X	o	X	o	o
4	X	X	o	X	o
5	X	o	o	o	X
6	X	X	X	o	o

FIG. d. Filtering scheme for the $(2N-1)\pi$ experiments. X indicate W_m terms that contribute to the evolution dimension spectrum. o indicate W_m terms that are averaged by the $(2N-1)\pi$ sequence and have no effect on the evolution dimension spectrum.

FIREMAT spectrum. If serious imperfections are found then the number of π pulses must be increased.

ACKNOWLEDGMENTS

This research was supported by the Department of Energy through Grant DE-FG03-94ER14453 and by the National Institute of Health through Grant GM08521-40.

REFERENCES

1. D. M. Grant, *in* "Encyclopedia of NMR" (D. M. Grant and R. K. Harris, Eds.), Vol. 2, Wiley, Chichester (1996).
2. Z. Gu, R. Zambrano, and A. McDermott, *J. Am. Chem. Soc.* **116,** 6368 (1994).
3. M. Strohmeier, A. Orendt, D. W. Alderman, and D. M. Grant, *J. Am. Chem. Soc.* **123,** 1713 (2001).
4. A. C. De Dios and E. Oldfield, *J. Am. Chem. Soc.* **116,** 11485 (1994).
5. J. R. Brender, D. M. Taylor, and A. Ramamoorthy, *J. Am. Chem. Soc.* **123,** 914 (2001).
6. J. Heller, D. D. Laws, M. Tomaselli, D. S. King, D. E. Wemmer, A. Pines, R. H. Havalin, and E. Oldfield, *J. Am. Chem. Soc.* **119,** 7827 (1997).
7. J. K. Harper, A. E. Mulgrew, J. Y. Li, D. H. Barich, G. Strobel, and D. M. Grant, *J. Am. Chem. Soc.*, in press.
8. D. H. Barich, D. M. Grant, R. J. Pugmuire, and R. J. Iuliucci, *J. Phys. Chem. A* **105,** 6780 (2001).
9. Y. Wei, D.-K. Lee, and A. Ramamoorthy, *J. Am. Chem. Soc.* **123,** 6118 (2001).
10. R. H. Havlin, D. D. Laws, H.-M. L. Bitter, L. K. Sanders, H. Sun, J. S. Grimeley, D. E. Wemmer, A. Pines, and E. Oldfield, *J. Am. Chem. Soc.* **123,** 10362 (2001).
11. D. W. Alderman, G. McGeorge, J. Z. Hu, R. J. Pugmuire, and D. M. Grant, *Mol. Phys.* **95,** 1113 (1998).
12. O. N. Antzukin, S. C. Shekar, and M. H. Levitt, *J. Magn. Reson. A* **115,** 7 (1995).
13. C. A. McDowell, *in* "Encyclopedia of NMR" (D. M. Grant and R. K. Harris, Eds.), Vol. 5, Wiley, Chichester (1996).
14. N. K. Sethi, D. W. Alderman, and D. M. Grant, *Mol. Phys.* **71,** 217 (1990).
15. N. Asakawa, M. Takenoiri, D. Sato, M. Sakurai, and Y. Inoue. *Magn. Reson. Chem.* **37,** 303 (1999).
16. C. Ye, R. Fu, J. Hu, L. Hou, and S. Ding, *Magn. Reson. Chem.* **31,** 699 (1993).
17. T. Kameda, N. Takeda, S. Kuroki, H. Kurosu, S. Ando, I. Ando, A. Shoji, and T. Ozaki, *J. Mol. Struct.* **384,** 27 (1996).
18. M. S. Solum, J. C. Facelli, Z. Gan, and D. M. Grant, *Mol. Phys.* **64,** 1031 (1988).
19. Q. Teng, M. Iqbal, and T. A. Cross, *J Am. Chem. Soc.* **114,** 5312 (1992).
20. Z. Gan and D. M. Grant, *J. Magn. Reson.* **90,** 522 (1990).
21. Z. Gan, *J. Magn. Reson.* **109,** 253 (1994).
22. M. M. Maricq and J. S. Waugh, *J. Chem. Phys.* **70,** 3300 (1979).
23. M. H. Levitt, *J. Magn. Reson.* **82,** 427 (1989).
24. The two to one doublets in the isotropic dimension consist of a continuous distribution of Lorentzian broadened lines. This massive overlap can neither be described accurately in the linear model required for TIGER nor be resolved by the TIGER protocol. Describing the observed inhomogeneous broadened lines with a homogeneous broadening mechanism leads to an incomplete isotropic separation of sideband manifolds (i.e., breakthrough).
25. R. R. Ernst, G. Bodenhausen, and A. Wokaun, "Principles of Nuclear Magnetic Resonance in One and Two Dimensions," p. 44, Clarendon Press, Oxford (1987).
26. C. P. Slichter, "Principles of Magnetic Resonance," 3rd ed., Springer-Verlag, New York (1990).
27. M. J. Potrzebowski, P. Tekely, and Y. Dusausoy, *Solid State Magn. Reson.* **11,** 253 (1998).
28. M. Strohmeier, D. Stueber, and D. M. Grant, manuscript in preparation.
29. G. McGeorge, D. W. Alderman, and D. M. Grant, *J. Magn. Reson.* **137,** 138 (1999).
30. A. E. Bennet, C. M. Rienstra, M. Auger, and K. V. Lakshmi, *J. Phys. Chem.* **103,** 6951 (1995).
31. H. Geen and G. Bodenhausen, *J. Am. Chem. Soc.* **115,** 1579 (1993).
32. D. W. Alderman, M. S. Solum, and D. M. Grant, *J. Chem. Phys.* **84,** 3717 (1986).
33. The fitting is done prior to replication. In order to allow for a comprehensible display of the results the data and model FIDs have to be replicated and Fourier transformed.
34. P. Hodgkinson and L. Emsley, *J. Chem. Phys.* **107,** 4808 (1997).
35. L. Werbelow, *J. Magn. Reson.* **67,** 66 (1986).
36. A. C. Olivieri, L. C. Frydman, and L. E. Diaz, *J. Magn. Reson.* **75,** 50 (1987).
37. J. Z. Hu, D. W. Alderman, and D. M. Grant, unpublished work.
38. O. N. Latzukin, Z. Song, X. Feng, and M. H. Levitt, *J. Chem. Phys.* **100,** 130 (1994).
39. R. A. Haberkorn, R. E. Stark, H. van Willigen, and R. G. Griffin, *J. Am. Chem. Soc.* **103,** 2534 (1981).
40. A. Naito, S. Ganapathy, K. Akasaka, and C. A. McDowell, *J. Phys. Chem.* **76,** 3190 (1981).
41. A. Naito and C. A. McDowell, *J. Phys. Chem.* **81,** 4795 (1984).
42. C. A. McDowell, A. Naito, D. L. Sastry, and K. Takegoshi, *J. Magn. Reson.* **69,** 283 (1986).
43. P.-G. Joensson and A. Kvik, *Acta Crystallogr. B* **28,** 1827 (1972).
44. A. Kvik, W. M. Canning, T. F. Koetzle, and J. B. Williams, *Acta Crystallogr. B* **36,** 115 (1980).
45. M. S. Lehmann, T. F. Koetzle, and W. C. Hamilton, *J. Am. Chem. Soc.* **94,** 2657 (1972).
46. M. Ramanadham, S. K. Sikka, and R. Chidambaram, *Acta Crystallogr. B* **28,** 3000 (1972).
47. H. Fuess, D. Hohlwein, and S. A. Mason, *Acta Crystallogr. B* **33,** 654 (1977).
48. The first evolution increment of a FIREMAT FID corresponds to a slow spinning MAS FID.
49. B. H. Suits, J. Šepa, and D. White, *J. Magn. Reson. A.* **120,** 88 (1996).